UC Riverside

UC Riverside Previously Published Works

Title

Soft material perforation via double-bubble laser-induced cavitation microjets

Permalink

https://escholarship.org/uc/item/5xh126m2

Journal

Physics of Fluids, 32(4)

ISSN

1070-6631

Authors

Robles, V
Gutierrez-Herrera, E
Devia-Cruz, LF
et al.

Publication Date

2020-04-01

DOI

10.1063/5.0007164

Peer reviewed

eScholarship.org Powered by the California Digital Library
University of California

ACCEPTED MANUSCRIPT

Physics of Fluids

This is the author's peer reviewed, accepted manuscript. However, the online version of record will be different from this version once it has been copyedited and typeset.
PLEASE CITE THIS ARTICLE AS DOI:10.1063/5.0007164

Soft Material Perforation Via Double-Bubble Laser-Induced Cavitation Microjets

V. Robles[1], E. Gutierrez-Herrera[1,2], L. F. Devia-Cruz[3], D. Banks[4], S. Camacho-Lopez[3], and G. Aguilar[1]*

[1] *Department of Mechanical Engineering, University of California, Riverside, Riverside, 92521, California, USA,*

[2] *Instituto de Ciencias Aplicadas y Tecnología, Universidad Nacional Autónoma de México, Ciudad de México 04510, México.*

[3] *Centro de Investigación Científica y de Educación Superior de Ensenada, Departamento de Óptica, Carretera Ensenada – Tijuana 3918, Zona Playitas, Ensenada, B.C., C.P. 22860, México*

[4] *Department of Mechanical Engineering, California State University Fullerton, Fullerton, CA, USA 92831*

**Corresponding author: gaguilar@engr.ucr.edu*

The resulting jet of two interacting laser-induced cavitation bubbles is optimized and studied as a technique for micro-scale targeting of soft materials. High controllability of double-bubble microjets can make such configuration favorable over single bubbles for applications where risk of ablation or thermal damage should be minimized such as in soft biological structures. In this study double-bubble jets are directed towards an agar gel-based skin phantom to explore the application of micro-scale injection and towards a soft paraffin to quantify targeting effectiveness of double-bubble over single-bubble jetting. The sharp elongation during the double-bubble process leads to fast, focused jets reaching average magnitudes of $U_{jet} = 87.6 \pm 9.9\, m/s$. When directed to agar, the penetration length and injected volume increase at approximately 250 µm and 5 nL per subsequent jets. Such values are achieved without the use of fabricated micro nozzles seen in existing needle-free laser injection systems. In soft paraffin, double-bubble jetting produces the same penetration length as single-bubble jetting, but with approximately a 45% reduction in damage area at a 3x greater target distance. Thus, double-bubble jetting can achieve smaller impact areas and greater target distances, potentially reducing collateral thermal damage and effects of strong shockwave pressures.

I. INTRODUCTION

Cavitation bubbles are relatively small and short-lived (micron spatial and microsecond temporal scales), but produce strong, localized mechanical, optical, chemical and thermal changes, making them prime candidates for micro targeting applications such as surface cleaning [1–3], cell targeting [4–8], and potential enhancement of localized heat transfer [9,10], among others. Specifically, cavitation has been exploited for the asymmetrical collapse that occurs in the vicinity of a boundary and forms a jet towards the target [11–14]. As will be explained in Section 2.3, the resulting jet magnitude depends on the dimensionless stand-off distance (γ) determined by 1) the bubble's maximum radius, and 2) the distance between the bubble initiation and the boundary (i.e. target distance). The former can be controlled by changing the focal spot size or varying the laser fluence by an attenuator, both of which can be experimentally restricting. Thus, the target distance is the single parameter that can feasibly control the jet speed in a wide range. However, close bubble-boundary proximities can result in unpredictable fast jets, unintended ablation, and exposure to high plasma temperatures and shockwave pressures (i.e. 6000-15,000 K and 2-6 GPa [15–17]) which lead to undesirable damage of the target surface. Lechner *et al*. computationally reported, that at close proximities ($\gamma \leq 0.2$), resulting jet speeds may surpass the field's previously accepted magnitude of ~100 m/s by reaching ~ 2000 m/s [18]. Additionally, Dijkink *et al.*, used cavitation shear forces to perforate cells for molecular intake; however at small γ, the cells central to the jet impingement region experienced decreased viability, likely due to thermal damage or detachment from intense pressures[4]. Furthermore, the jetting behavior of a bubble near a boundary is influenced by the surface properties. Particularly in the field of medical laser applications, some researchers describe complex bubble dynamics while observing the interaction and behavior of cavitation bubbles near elastic boundaries (emulating mechanical properties of tissue) [19–23]. Thus, it is essential for many applications to effectively increase γ thereby minimizing detrimental effects, while maintaining the required range of jet speeds for the application of interest and removing strong dependence on a present target and its properties. A technique to generate jets without the need of a boundary or fabricated device is to utilize two neighboring cavitation bubbles [24–26]. Thus, the interaction of two bubbles may provide a unique method to increase γ and enhance the controllability of fast jets to open viable avenues for applications of tissue cutting, lithotripsy and needle injection alternatives.

Traditionally, needle injections have been proven effective; however, sources of contamination, large volumes of medical wastes among phobias have driven the search for alternatives such as piezoelectric actuator-driven jets [27], spring driven jet injectors [28] and laser-based systems [29–33], the latter having gained attention for greater controllability. Laser-based injection systems principally operate with jets formed by displacing a liquid through a micronozzle[34] with the growth of a thermocavitation bubble. However, the

AIP Publishing

ACCEPTED MANUSCRIPT
Physics of Fluids
This is the author's peer reviewed, accepted manuscript. However, the online version of record will be different from this version once it has been copyedited and typeset.
PLEASE CITE THIS ARTICLE AS DOI:10.1063/5.0007164

requirement of tapered micronozzles and channels call for complex fabrication and are prone to clogging, thus reducing reproducibility. Continuous wave laser methods [30,35,36], typically use a corrosive copper nitrate solution because the incident wavelength should be strongly absorbed to initiate thermocavitation; -a thermal process in which an explosive phase transition occurs [9,37,38]. In this case, the liquid faces relatively long heating stages (i.e. tens of milliseconds) which may chemically change and deem the drug ineffective. Methods to tackle this issue have been proposed by separating the cavitating liquid from the drug with a flexible membrane [39], but the device's fabrication is further complicated. Additionally, thermocavitation occurs quasi-periodically, with random jitter in bubble initiation times and bubble sizes at low powers [37], making the volume of injection only partially predictable. Thus, pulsed laser-induced bubbles remain superior for controllability and their capability to be generated in transparent media with short lived, minimal heating (<1.3 ms, and < 12.8 °C [40]). To the best of our knowledge, the possible effectiveness of using double-bubble jetting for needle-free injection has not been explored. Neighboring cavitation bubbles generated by pulsed lasers may allow for fast jets to be initiated without the need for fabricated nozzles or relying on absorbing solutions and with minimal localized heating.

In the presented work, we analyze the effects of spatial and temporal separations of double-bubble configurations, on the resultant jet speed. At optimized parameters, we direct fast jets towards soft materials to show the potential of double-bubble arrangements to replace single-bubble jetting in applications of micro-targeting. Single- and double-bubble arrangements are compared by characterization of the damage sites (penetration lengths and areas) resulting from the two processes. Furthermore, the possible application of double-bubble configurations for needle-free injections is considered by exploring the formation of cavities in agar-gel phantoms.

II. MATERIALS AND METHODS

A. Bubble Generation and Imaging of Jet Dynamics

Two 1 mm diameter sized bubbles were generated in deionized (DI) water using two Q-switched Nd: YAG lasers (EKSPLA NT 342, Vilnius, Lithuania and Continuum Surelite SLII-10, California, USA) with 1064 nm wavelengths, and 6 ns pulse duration. As shown in Figure 1, the beams were individually collimated and focused antiparallel with matching aspheric lenses (f = 11 mm) into a glass cuvette containing DI water. The X-axis alignment provided the highest temporal resolution for analyzing the jet dynamics. Each laser's energy was individually adjusted with an attenuator composed of a half wave plate (1/2 WP) and polarizing beam splitter (PBS) such that the bubbles were of similar size regardless of miniscule differences between beam profiles. The experiments were conducted with approximately 1 mJ energies. The energies were measured following sets of experiments before the cavitating lenses (f_1 and f_2) using a Gentec-EO energy meter (QE25LP-S-MB-QED-D0, Oregon, USA).

The bubble interaction and jetting dynamics were studied using high speed (HS) shadowgraphy at 193,771 frames per second (fps) and 48 x 256-pixel resolution using a HS Phantom camera (Miro M310, USA) coupled with a long-distance Infinity microscope (KC VideoMax, IF-3 Objective, USA). The imaging resolution (~22 µm per pixel) averaged over the elapsed time per frame accounts for an uncertainty in average velocity measurements of 2.1 m/s. The events were back-illuminated with a diffuse white light source. The camera resolution was reduced to 64 x 48-pixels to accurately measure a single bubble's expansion time at an enhanced rate of 3.8 x 10^5 fps. A Berkeley Nucleonics pulse delay generator (PDG) (M-555, California, USA) was used to externally synchronize and trigger both lasers and HS camera up to a 1 ns resolution (refer to Figure 1).

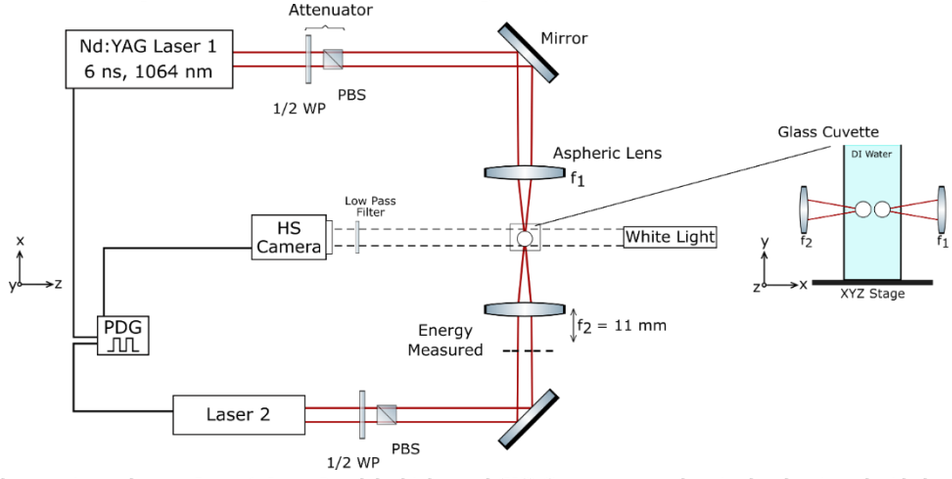

Figure 1. A schematic of the experimental setup. Laser 1, Laser 2 and the high speed (HS) Camera are synchronized and activated with the pulse delay generator (PDG). Laser 1 and Laser 2 energies are controlled by attenuators. Inset depicts lateral view of the cuvette setup used for imaging of jetting dynamics.

ACCEPTED MANUSCRIPT
Physics of Fluids
This is the author's peer reviewed, accepted manuscript. However, the online version of record will be different from this version once it has been copyedited and typeset.
PLEASE CITE THIS ARTICLE AS DOI:10.1063/5.0007164
AIP Publishing

B. Target Preparation

Two target materials were used to 1) characterize and compare the damages from single-bubble jetting (SBJ) and double-bubble jetting (DBJ), and 2) explore DBJ as a proof of concept for needle-free injection. First, a soft paraffin (i.e. Petroleum Jelly, Vaseline) was used for its hydrophobicity and malleability, allowing to characterize the damage areas and penetration lengths of jet impingement. Approximately 150 mg of soft paraffin was applied onto 1 x 2 cm glass substrates and slowly heated to 60 ℃ until the soft paraffin liquified and became transparent. The samples were cooled to room temperature and solidified on the glass as smooth 500 µm thick layers. Once solid, the samples became semi-opaque, preventing real time lateral view of the impingement process. Additionally, the soft paraffin's semisolid viscous properties could not accurately portray the material properties of soft tissue for applications of injection. Thus, an optically transparent agar gel was used as a tissue phantom model for its comparable mechanical properties (Young's modulus) to tissue. A concentration of 1% agar was chosen as it provides a Young's Modulus of $E \sim 20$ kPa [41], comparable to the lower limit of skin's modulus [42]. The agar samples were prepared with 1:100 ratio of Molecular Genetics agar powder (BP1423, Mexico) to DI water by weight. The mixture was continuously mixed and heated to 90 ℃ until the powder was dissolved, and no granules were observed. The solution was then poured into open-ended cuvettes and cooled to 4 ℃, solidifying into smooth 1 cm^2 rectangular prisms.

C. Double-Bubble Jetting Parameters

Figure 2 shows a depiction of two subsequent neighboring cavitation bubbles resulting in the formation of a slow bulk motion countered in the opposite direction by a thin high-speed jet. As the second initiated bubble (B_2) grows, it is elongated by the contraction of the first bubble (B_1) (see Figure 2b). The final moments of B_1 coincide with the start of collapse of B_2 which is accelerated by the second emitted pressure wave of B_1 causing the elongated cone to invert and form a focused jet [24,25] (refer to Figure 2c). B_1 completes its collapse and rebounds in the opposite direction. The direction of the narrow jet of B_2 can be predetermined from the axis of the two bubbles, whereas the speed can be modified by the relative bubble sizes, initiation times, and spatial separations. The target distance can also be varied to achieve different impinging areas and penetration lengths.

To efficiently compare the micro-targeting effectiveness of a double-bubble arrangement to that of a single-bubble, the effects of spatial and temporal parameters on double-bubble jetting speeds were explored. The relative bubble sizes could be expressed as the ratio $\rho = R_{max,2}/R_{max,1}$, where $R_{max,2}$ and $R_{max,1}$ represent the maximum radii that each bubble would reach in an isolated state. For simplicity, this study was conducted with same sized ~1 mm diameter bubbles ($\rho = 1$). First, the relative bubble-bubble (BB) initiation phase (τ) was fixed to analyze the effects of BB spatial separation on jet speeds. The BB initiation phase is defined by Equation 1,

$$\tau = \frac{\Delta t}{T_{exp,1}}, \tag{1}$$

where Δt is the temporal delay between the generation of each bubble and $T_{exp,1}$ is the expansion time of B_1. Considering $\rho = 1$, T_{exp} is the same for B_1 and B_2 and equal to half of the bubble lifetime which can be measured from optical breakdown (i.e. plasma emission) to the end of bubble collapse [43]. The average bubble expansion time was $T_{exp} = 55 \pm 1.3$ µs. B. Han *et al.* numerically investigated jets produced by pairs of micro bubbles and described two distinct processes: in-phase ($\tau = 0$) and antiphase bubbles ($\tau = 1$). Using computational methods, they reported that for same sized micron-scaled bubbles ($\rho = 1$) a single optimal phase exists ($\tau = 1$) for producing fast jets regardless of BB spatial separation [24]. A change in the optimum BB phase is not expected for millimeter sized bubbles when compared to micron sized bubbles because the decrease in surface tension for larger cavities will affect the magnitude of the induced pressures not the time of pressure formation relative to the bubble collapse [44]. Thus, this study began with determining the optimum BB spatial separation for antiphase (τ = 1) millimeter sized bubbles. The dimensionless spatial bubble-bubble separation (γ_{BB}) can be expressed as

$$\gamma_{BB} = \frac{D_{BB}}{R_{max,1} + R_{max,2}}, \tag{2}$$

where D_{BB}, is the spatial separation between the bubble initiation centers (see Figure 2a). The BB dimensionless separation is varied from $\gamma_{BB} = 0.55$ to 1.0 by translating one aspheric lens with respect to the other (f_1 and f_2, refer to Figure 1). After determining the optimum BB spatial separation, the effect of BB phase generation on the jet speed was confirmed by carrying out ten temporal delays in 5 µs increments. The phase experiments were conducted using the optimal BB spatial separation and a second arbitrary separation to experimentally test the dependency of the optimum BB phase on BB spatial separations.

Upon determining the optimum temporal and spatial conditions, the effects of the stand-off distance to a specified target on the damages produced were explored. The dimensionless bubble-target distance (γ_{BT}) is defined by

$$\gamma_{BT} = \frac{D_{BT}}{R_{max,2}}, \tag{3}$$

ACCEPTED MANUSCRIPT
Physics of Fluids
This is the author's peer reviewed, accepted manuscript. However, the online version of record will be different from this version once it has been copyedited and typeset.
PLEASE CITE THIS ARTICLE AS DOI:10.1063/5.0007164
AIP Publishing

where the bubble-target (D_{BT}) spatial distance is normalized by the maximum radius of the closest generated bubble (see Figure 2c).

The resulting leading edge of the jets was tracked to estimate average speeds from the first sight of jet formation. Speed measurements via leading edge tracking provided low-end estimates because, there is a loss of liquid momentum as the gas drives the jet motion [12]. Upon finding the optimal BB parameters, the jets were directed towards soft paraffin and agar. Due to experimental limitations, the double-bubble arrangements for material targeting were reoriented on the Y-axis as seen in Figure 2. The soft paraffin and agar targets (i.e. samples) were immersed in the DI water on the top and floor of the cuvette respectively. The malleable soft paraffin was placed on the top edge to avoid smearing on the cuvette and preserve the sample's flat profile. The agar was placed on the floor of the cuvette as this position allowed for the highest stability of the sample. The target-cuvette assembly was translated by an XYZ stage to vary the position of the bubbles relative to the edge of the target. Cavities formed in soft paraffin were approximated as circular and characterized by the radii and penetration lengths using ImageJ to analyze images obtained using an optical microscope (20x magnification, Meiji Techno, Japan). The penetration lengths in agar phantoms were measured using ImageJ and high-speed image sequences.

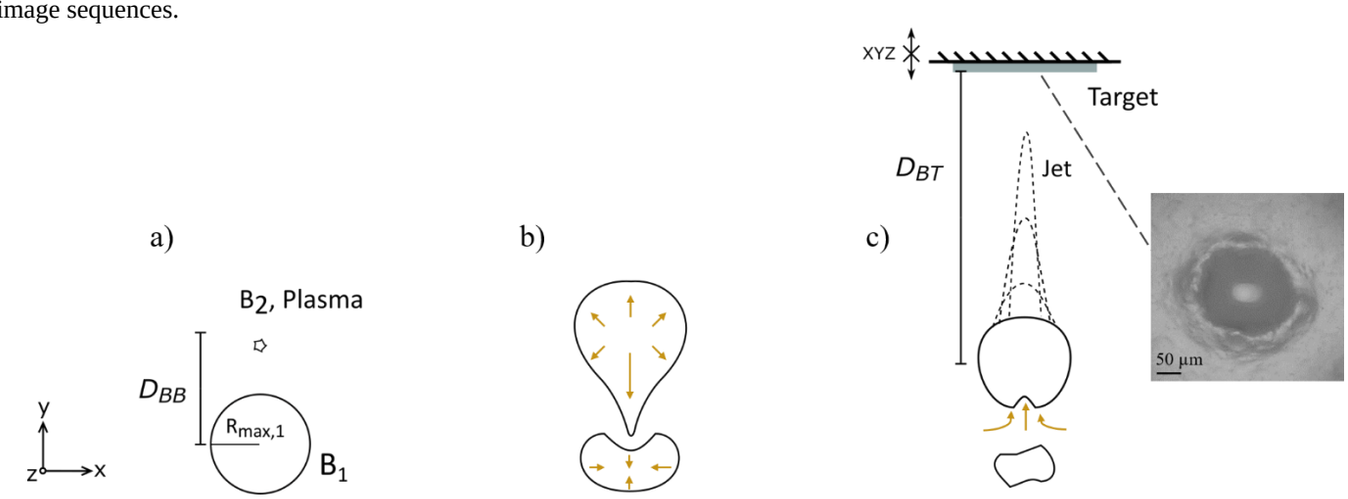

Figure 2. Camera point of view of target setup and depiction of DBJ process. a) Formation of B_2 at maximum size of B_1 with spatial separation D_{BB} b) elongation of B_2 formed by contribution of B_1 collapse. c) Reversal of conical edge and propagation of jet. Inset shows a typical damage formed by a jet impingement on soft paraffin.

III. RESULTS AND DISCUSSION

A. Effects of Bubble-Bubble Separation and Phase Initiation on Jet Velocity

The jet speeds are first studied at varying relative distances while maintaining the BB temporal delay constant at $\tau = 1$. The bubbles are isolated from boundaries at approximately $5R_{max}$ from the closest cuvette wall and oriented in the X-axis as seen in Figure 1. Figure 3 shows four sequences of antiphase bubbles interacting at BB separations of $\gamma_{BB} =$ 0.63, 0.74, 0.85, and 1.07. The captured images of bubbles and jets appear as black shadows due to the refraction of incoming light in the water-gas interface. To understand the formation of jets in antiphase bubbles, attention is first placed on the most defined case of $\gamma_{BB} = 0.74$ (see Figure 3b). In the case of antiphase bubbles, B_2 is initiated at B_1's maximum size and the overlap between B_1's collapse stage and B_2's growth stage forms an elongation in B_2 representing a conical shape towards B_1 (most noted in Figure 3b at 15.5 µs). The inflow of liquid between the bubbles forms a high pressure region as reported in the simulations of B. Han [24]. As B_2 begins to collapse, B_1 has completed its collapse stage and due to its rapid decrease in volume a high-pressure compressive wave is emitted [16,45] surrounding the tip of B_2 and further driving its collapse. The sharp coned-wall of B_2 inverts and collapses at a faster acceleration than the opposing bubble wall [44] causing a net radial inflow in which a jet forms and travels through the bubble in a toroidal shape piercing the opposite bubble wall. Simultaneously, an opposing unfocused bulk flow emerges from B_1.

When the bubbles are too close (Figure 3a) B_2 elongates asymmetrically during its growth, but its proximity causes it to penetrate through the walls of B_1 interfering with the jetting process due to the fractional coalescing of the two bubbles. Upon the start of collapse of B_2, however, the elongated curved edge still reverses and forms an outward unfocused flow as seen in Figure 3a, 46.4 µs onward. When the bubbles are more distant, as in Figure 3c, the stretching of B_2 occurs without physical contact with B_1, but the elongation is not maximized (see Figure 3c, 31 µs) and the interaction is weakened. As the bubbles are distanced further, as in Figure 3d, their behavior begins to resemble isolated cavitation events with minor opposing flows. The effect of the separation is easier realized by plotting the speed over time as seen in Figure 4.

ACCEPTED MANUSCRIPT
Physics of Fluids
This is the author's peer reviewed, accepted manuscript. However, the online version of record will be different from this version once it has been copyedited and typeset.
PLEASE CITE THIS ARTICLE AS DOI:10.1063/5.0007164

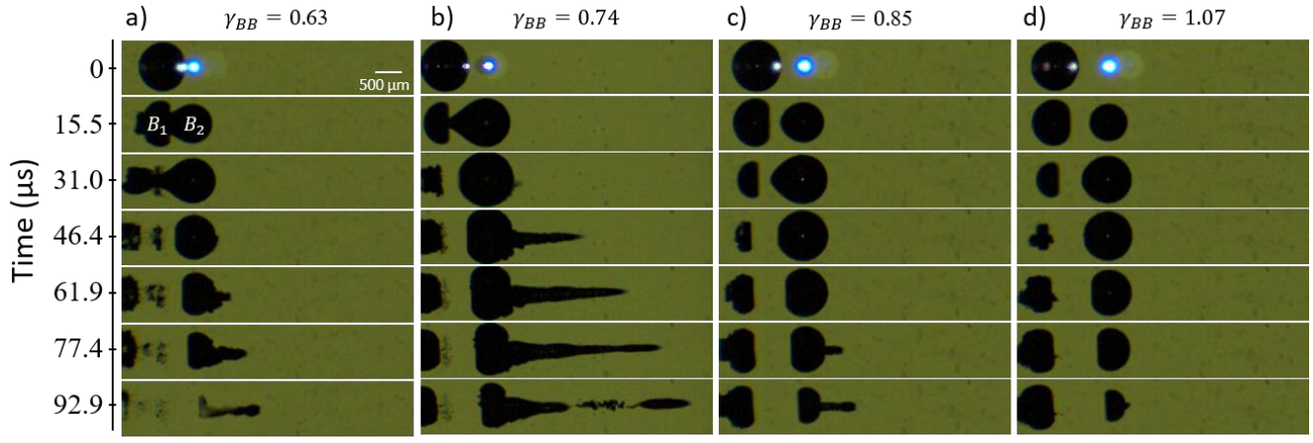

Figure 3. Image sequence of four bubble-bubble spatial separations: γ_{BB} = a) 0.63, b) 0.74, c) 0.85, and d) 1.07 (each at τ = 1). The first image (time 0) shows the moment that Laser 2 is fired.

Figure 4 plots the speeds of the emerging jets of Figure 3 starting from the first sight of bubble protrusion. At the furthest conducted separation of $\gamma_{BB} = 1.07$, no concentrated fluid motion is seen until after 90 µs of bubble initiation and thus, is not plotted. Figure 4a shows the jet evolution for the optimal BB spatial separation (refer to Figure 3b) and equal displacement of bubbles closer to and further from each other by a change of $\Delta\gamma_{BB}$ = 0.11. The overlapping profile speeds of 0.63 and 0.85 in Figure 4a suggest that the jet is diminished similarly for displacement above and below the optimum BB separation of $\gamma_{BB} = 0.74$. However, the jets do not emerge at the same time; smaller bubble separations produce jets at an earlier time due to the shorter distance the jet must travel to reach the opposite bubble interface. Figure 4b shows the maximum jet speed for different γ_{BB}. An optimal γ_{BB} occurs at 0.74, and the effect on BB separation appears symmetric for the range of this study. In this case, the maximum averaged measured velocity of U_{max}= 87.6 ± 9.9 m/s is achieved within 5 µs of jet formation and converges to U_{conv} ~25 m/s within 80 µs. We experimentally verified the assertions in Ref. [24] that antiphase bubbles (τ = 1) produce the fastest jets regardless of a different bubble scale and independent of BB separation. These experiments are included in Appendix A. The BB separation and phase are kept constant at $\gamma_{BB} = 0.74$ and $\tau = 1$ for the remainder of the experiments.

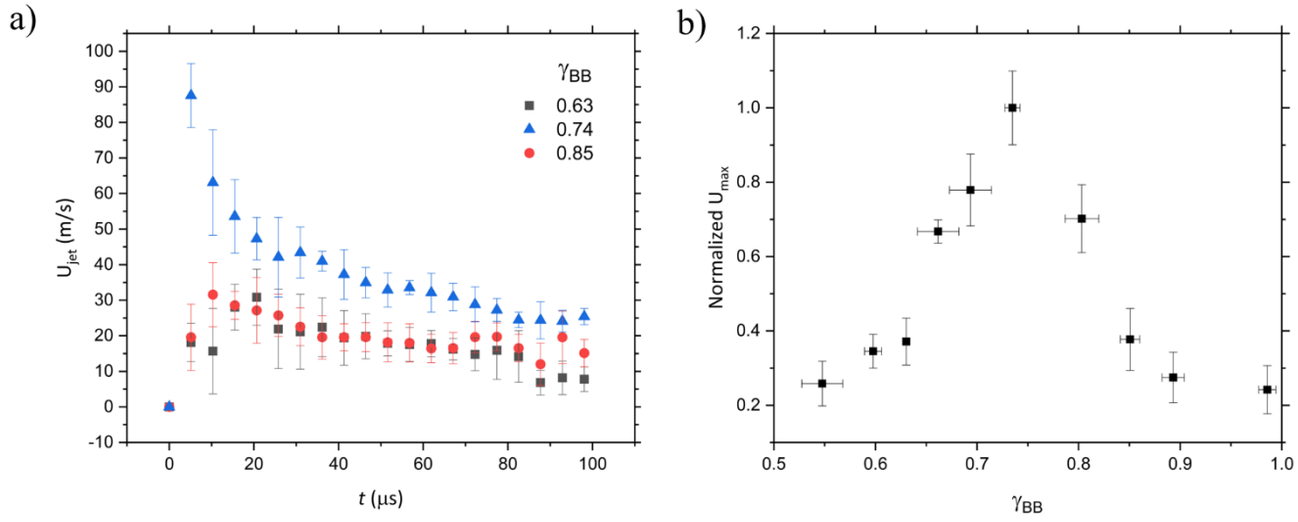

Figure 4. a) Jet speed with respect to time of jet formation for three different BB separations (γ_{BB}) at τ = 1, ρ = 1. b) Normalized maximum jet speed for various BB separations.

B. Penetration Length and Damage Radius vs Bubble-Target Stand-off in Soft Paraffin

To demonstrate the extent that DBJ can outperform SBJ in existing applications such as surface cleaning or cell targeting, sites generated by each configuration's jets impinging onto a soft paraffin were compared. As mentioned in section 2, the bubbles were reoriented onto the Y-axis. The effect of gravity is negligible as shown by the Froude number (ratio of inertial and gravitational forces), U_{jet}^2/gL, where U_{jet} is the jet velocity, g is the acceleration due to gravity and L is the characteristic length. Taking the jet velocity as

ACCEPTED MANUSCRIPT
Physics of Fluids
This is the author's peer reviewed, accepted manuscript. However, the online version of record will be different from this version once it has been copyedited and typeset.
PLEASE CITE THIS ARTICLE AS DOI:10.1063/5.0007164
AIP Publishing

the optimum converged speed (U_{conv} ~25 m/s) and characteristic length as the length of the jet at the furthest measured point (L = 1.75 mm), the Froude number is on the order of 35 x 10^3 which confirms that the jet's inertial forces are dominant for the specified scales. Additionally, experimental tests of Y and X-axis BB orientations produced comparable average jet speeds within uncertainties of the measurements (Y jet speeds are not shown).

Figure 5a and 5b show dynamics and damages of SBJ and DBJ impingement onto soft paraffin, each reaching comparable penetration lengths of roughly 110 µm. The sequences show three moments: 1) the maximum bubble growth (B_2 in DBJ arrangement), 2) the time of impact onto the soft paraffin, and 3) the maximum size of the rebound bubble. The resulting damages are fitted to a circle and characterized by the radius as seen in Figure 5a. In each arrangement, the jet removes clusters of material upon impact, but due to the properties of the soft paraffin and the radial shear outflows at the material surface, the jet primarily pushes the material outward creating a raised ring-like shape. By comparing the point-of-impact images (Figures 5a, @ 61.2 µs and 5b, @ 32 µs), the difference in jet widths upon impingement is noted; DBJ results in a finer jet. The difference in the jet dimensions can be attributed to the curvature of the bubble before the jet is formed (may also be affected by distance to target). The dashed lines in Figures 5a and 5b at 0 µs outline the curvature of the opposite bubble wall which inverts in a toroidal shape and becomes the leading edge of the jet. The asymmetrical geometry of each case (boundary on one side for SBJ and bubble on the opposite side for DBJ) cause an elongated growth and due to surface tension, the bubble walls with the highest curvature implode faster[17]. The feature of higher curvature in DBJ seems to lead to a finer jet capable of larger penetration lengths than SBJ as seen in Figure 6. The rebound bubbles also play a role in the formation of the damage. Particularly in SBJ cases near $\gamma = 1$, following the first collapse of the cavitation bubble, the rebound is attached to the target and the bubble regrows highly asymmetrically along the wall (see Figure 5a, 79.2 µs), further enlarging the damage radius. This rebound damage contribution is not present in the case of DBJ because the successive regrowth and collapse occur off-site away from the surface (noted in Figure 5b @ 80 µs).

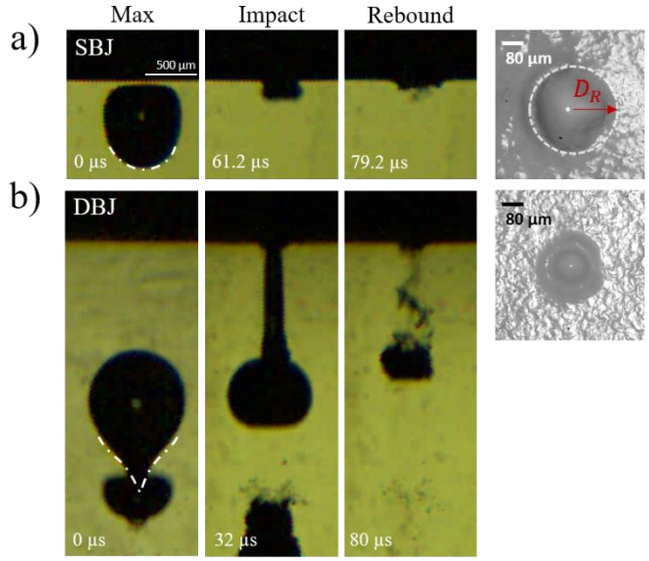

Figure 5. Jetting dynamics and soft paraffin damage radius for a) single ($\gamma = 0.96$) and b) double-bubble jetting (τ = 1, ρ = 1, γ_{BB} = 0.75).

Figure 6 shows the penetration length (L_P) and damage radius (D_R) for both SBJ and DBJ at various bubble-target stand-off distances. Damage sites resulting from single bubbles can be observed up to approximately $\gamma_{BT} = 1.4$, in which both the damage lengths and radius from single bubbles follow a similar trend: the values increase parabolically as the stand-off distance approaches a value of $\gamma_{BT} \approx 1.1$. After $\gamma_{BT} \approx 1.1$, the lengths and radii begin to decrease. In the range of SBJ experiments, the damage radius is consistently larger than the penetration lengths achieved which may be unfavorable for various applications such as needle-free injections. The effect of using DBJ for inducing damage sites shows two notable differences when compared to SBJ damage sites. First, DBJ can produce damages at larger stand-off distances up to $\gamma_{BT} = 4.2$. Additionally, in the range of ($1.75 < \gamma_{BT} < 3.8$), the damage radii are smaller than the penetration lengths thus generally making DBJ a more suitable technique for localized targeting in scenarios that require smaller impact radius-to-length ratios. Stand-offs outside this range generate similar damage sites as those seen SBJ, that is, the damage radii surpass the penetration lengths. As the stand-off is decreased from $\gamma_{BT} = 1.4$, both the damage radii and penetration lengths begin to decrease following a similar trend as $\gamma_{BT} < 1.1$ for SBJ. As the DBJ arrangement is moved closer to the soft paraffin target, a larger portion of the jet (radially out from the central axis) has sufficiently high velocity to deform the target in a larger region. Additionally, a vortex flow occurs when the jet impinges on the target which provides a shear stress that further enlarges the damage radius. In the largest observed stand-offs, the average damage radius and penetration lengths are within uncertainty. In the

ACCEPTED MANUSCRIPT
Physics of Fluids
This is the author's peer reviewed, accepted manuscript. However, the online version of record will be different from this version once it has been copyedited and typeset.
PLEASE CITE THIS ARTICLE AS DOI:10.1063/5.0007164

specific case of Figure 5a and 5b, the damages of each configuration are compared. To achieve the same average penetration length of approximately 110 µm, γ_{BT} of double-bubble jetting can be on average 3 times larger than that of single bubble jetting. Additionally, the damage surface profile is about 45% smaller for the DBJ configuration.

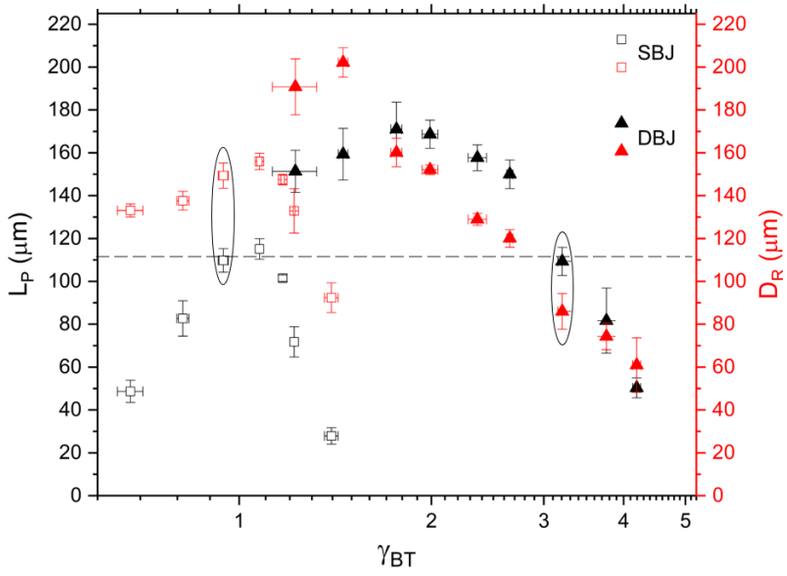

Figure 6.Penetration length and damage radius for single- and double-bubble jetting at varying bubble-target distances. Dotted line runs across similar-sized penetration lengths for cases in Figures 5a 5b. Measurement of penetration length starts from initial surface base.

C. Penetration Length vs Number of Jet Impingements in Agar-gel Phantom

To observe the effect of multiple successive jets from a double-bubble jetting arrangement, emerging jets were directed towards soft paraffin and an agar-gel phantom. Figure 7a shows lateral sequences of jet propagation into agar for different number of jets (J_i, where i = 1, 3 and 5 jets) on the same spot. The jet is first seen to penetrate the agar in J_1, at 10.4 µs and propagates through 41.6 µs. Upon penetrating the agar interface, the jet's shadow appears thinner as only the core of the jet provides enough pressure to cause failure in the agar. However, in subsequent jets J_3 and J_5, the propagating jet inside the agar is notably wider due to the preexisting guide of cavities formed from previous jets. Additionally, the jet penetrates further after each successive jet. In all cases, upon the collapse of B_2 (Figure 7a, row 41.6 µs), the jet inside the agar seems to vanish. The gaseous blanket surrounding the jet has condensed and recombined with the liquid whose refractive index closely matches that of the agar target.

Figure 7b shows the penetration lengths achieved with various successive number of jets for double-bubble jetting onto agar and soft paraffin. The experiments are conducted in the soft paraffin with the purpose of showing the trend in a different material. Each point in the plot corresponds to the average penetration length achieved by three repetitions of different number of jets varying between 1 jet to 8 jets. The temporal separation of subsequent jets is on the order of about 10 seconds, large enough for initial conditions to restore after each jet. A stand-off of $\gamma_{BT} = 3.5$ was chosen for both materials as it is sufficiently distanced enough to allow for estimating the impact jet velocity, but not large enough for the penetration area to have a large aspect ratio (radius/penetration length) as seen in Figure 6. A linear relation can be fitted onto both materials up to the first 5 jets, with a slope of 250 µm/jet and 40 µm/jet for agar and soft paraffin respectively. The first jet punctures the agar with a pilot cavity which then serves as a guiding channel for successive jets. The penetration length is approximately linear during the first 5 jets and begins to plateau with additional jets generating smaller growths. The plateau can be attributed to keeping the base plane constant, regardless of the local γ_{BT} stand-off distance increasing in the impact region after each jet. After 5 jets, the flow's momentum is decelerated resulting in smaller and more variable impact pressures as seen in the corresponding growth of the standard deviations in Figure 7b. At larger number of jets, the length will remain constant unless the bubble-target distance is readjusted after each jet. The plot for soft paraffin, although not achieving the same lengths, provides a similar linear trend for approximately the first 5 jets.

ACCEPTED MANUSCRIPT
Physics of Fluids
This is the author's peer reviewed, accepted manuscript. However, the online version of record will be different from this version once it has been copyedited and typeset.
PLEASE CITE THIS ARTICLE AS DOI:10.1063/5.0007164

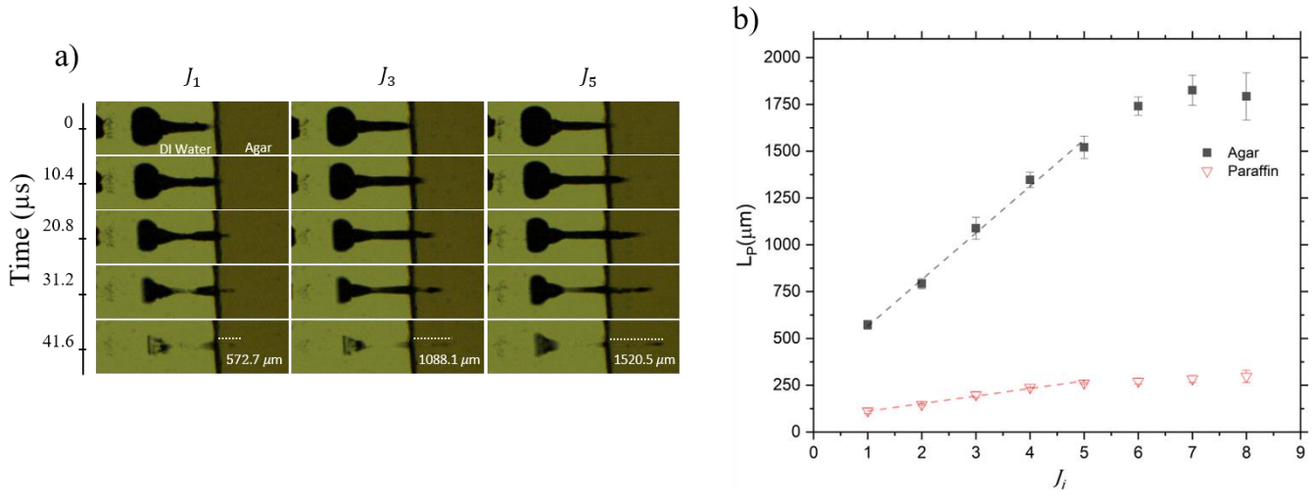

Figure 7. a) Lateral view of jet propagation in 1% agar using J_i = 1, 3 and 5 DBJ jets in the same region. b) Penetration length on agar and soft paraffin as a function of number of impacting jets (J_i) (τ = 1, ρ = 1, γ_{BB} = 0.75, γ_{BT} = 3.5). Each point in the plots represent the average of 3 experiments.

Although the effect of the jet can be quantified by the resulting penetration lengths and damage radius, the principal contributors to the effects achieved are the jet velocity, and elastic modulus of the target. The impact pressure P_{jet} of the jet that causes the failure in the sample is calculated by

$$P_{jet} = \frac{1}{2}\delta U_{jet}^2, \quad (4)$$

where δ is the water density, and U_{jet} is the jet velocity [46]. The mechanical stress applied by the jet pressure must exceed the elastic modulus (E) of the target of interest for failure to occur. K. Cu *et al.* defined the penetration strength ratio $S = P_{jet}/E$ to indicate the potential of target rupture (if S > 1) [47]. At a stand-off of γ_{BT} = 3.5, the DBJ average impact velocity is U_{jet} = 32 m/s and provides an impact pressure of 512 kPa, and an approximately penetration strength ratio of 25 for a sample of 1% agar. Such penetration strength signifies that the discussed setup can afford to penetrate a stiffer material, or, the stan-off distance may be further increased.

The cavities formed in the agar phantoms can be approximated as conical shapes to estimate the injection volumes achieved. For J_5, the radius of the cavity D_r (measured from the images in Figure 7), is approximately 125 μm at the entrance (measured at 20.8 μs because of higher contrast) and the penetration length is about 1.52 mm. Using the volume of a cone, $V = L\pi {D_r}^2/3$, where L is the penetration length, and D_r is damage radius of the cavity, the approximate injected liquid amounts to 25 nL (or 5 nL per jet until 5 jets) which is on the lower-end for required dosages of typical applications (vaccines, antibiotics [48]). To compare the effectiveness of this technique with other needle-free methods, the injection efficiency, defined by the ratio of jet kinetic energy to the input energy required to generate the jet, is found. Table 1 compares the performance of DBJ to other laser-based injection methods.

TABLE I. Comparison between laser-based injection systems.

Method	Apparatus	U_{max} (m/s)	Volume/Penetration per Injection	ϵ_{energy} % [a]	Optical Energy (mJ)	Ref.
Thermocavitation (450 nm, 0.5 W, 1 ms)	Chamber: D 120 μm, L 700 μm Nozzle: D 120 μm	-	20.2 nL/ 1.2 mm	0.32	5	[35]
Pulsed cavitation and ablation (2940 nm, 1085 mJ, 150 μs)	Chamber: H 11 mm Nozzle: D 150 μm	120	350 nL, 3.5 mm (10 % polyacrylamide gel, ~60 kPa)	0.21	1085	[39]
Thermocavitation (790 nm, 116 mW, 500 ms)	Chamber: D 120 μm, L 200 μm Nozzle: D 50 μm	94	~40 nL/ 675 μm (1% agarose, ~15 kPa [49])	0.07-0.14	58	[30]
Pulsed cavitation (1064 nm, 1 mJ each, 6 ns)	None	87	~5 nL/ 570 μm (1% agar, ~20 kPa [41])	0.13	2	This work

ACCEPTED MANUSCRIPT

Physics of Fluids

This is the author's peer reviewed, accepted manuscript. However, the online version of record will be different from this version once it has been copyedited and typeset.
PLEASE CITE THIS ARTICLE AS DOI:10.1063/5.0007164

[a] Injection efficiency: jet kinetic energy transferred to the material per energy supplied to injectors [35]. $\epsilon_{energy} = {KE}/{E_{laser}}$.

As seen in table 1, the injection efficiency by energy is on the lower limit of other laser-based injection systems. However, this efficiency depends on the modulus of the sample, which is lower than those in references [35,39] but higher than reference [30]. One advantage of DBJ over previous laser-based jetting systems is the absence of required microfabricated devices. Such complex microchannels and nozzles are prone to clogging which can decrease jet controllability overtime. Moreover, existing continuous wave systems superheat the jetting fluid for several microseconds before cavitation is initiated[9,37], possibly changing the molecular structure of medication. Such issue is limited to short lived and localized heating[40], but can be further avoided by generating the double-bubble jets in a separate medium and transferring the momentum to the medicine. Additionally, to further enhance the injection efficiency of DBJ to be useful for needle-free injection purposes, the addition of tapered nozzles could be explored. However, due to the fast jets without additional apparatus, such added nozzle would not be required to be micron-scaled as those in table 1 and thus less prone to damage.

IV. CONCLUSION

We analyzed the microjet effect on soft materials due to spatial and temporal separation between a double-bubble arrangement. The dynamics of two neighboring bubbles are explored to compare the effectiveness in which double-bubble jetting (DBJ) may be more beneficial in applications of localized targeting that currently use a single-bubble jetting (SBJ). A double-bubble arrangement allows for higher degrees of freedom for controlling jet dynamics when compared to only one parameter with single-bubbles. The critical parameters of bubble-bubble temporal and bubble-bubble spatial initialization were found to be τ = 1 and γ_{BB} = 0.74, respectively. The phase of τ = 1 allowed for the same sized bubbles to align B_1's pressure emission upon collapse with the beginning of B_2's collapse which formed a constructive interaction leading to an average maximum jet velocity of $U_{jet} = 87.6\ m/s \pm 9.9\ m/s$ At the critical BB separation, the bubbles were close enough to have a strong, constructive interaction with the present pressure fields, but far enough to not interfere with the other bubble's dynamics. With these critical conditions, DBJ proves to be superior to SBJ when considering penetration lengths versus impact region. The same penetration length in soft paraffin can be achieved using single and double-bubble jetting, but at safer (~3x larger) stand-off distances and minimized surface damages (by about 45%) for double-bubble configurations. Particularly, the advantages of DBJ over SBJ can be attributed to two contributing features. First, the DBJ arrangement seems to lead to a sharper elongation translating to a finer jet upon impingement. Additionally, due to larger initial target separations in DBJ, the rebound bubble does not reach nor contribute to the damage site. Further, the DBJ configuration was directed onto a 1% agar-gel phantom as a proof of concept for needle-free applications. Successive jets into the gel led to a linear increase in the penetration length up to 1.5 mm after 5 jets with a volume of 25 nL. Double bubble arrangements may be compact, device-free alternatives for needle-free applications, but further studies are required to fully understand the resulting process. Particularly, the degree and effect of possible vapor entrainment into the formed cavity is not understood. Furthermore, factors governing jet formation namely, relative bubble ratios, solution surface tension and viscosity remain to be studied to determine their effects on achieved penetration lengths.

ACKNOWLEDGEMENTS

The authors would like to thank Juan Carlos Gonzalez Parra for laboratory assistance and fruitful discussions. V. Robles was funded by the Ford Foundation Predoctoral Fellowship.

DATA

The data that supports the findings of this study are available within the article.

APPENDIX A

Figure 8 shows typical jet evolutions of four phase separations (τ = 0, 0.54, 1, and 1.44) at a BB spatial separation of γ_{BB} = 0.74. For simultaneous generations, as seen in Figure 8a, each bubble behaves like a single bubble acting on a nearby solid boundary. That is, the bubbles are attracted to each other, but in distinction, a thin liquid layer is formed between the gaseous cavities until coalescing occurs at the beginning of the rebound bubbles (Figure 8a @ 154.8 μs). No outward focused jet formation is observed due to the destructive interference of the equal and synchronized opposing pressure waves.

As the phase difference increases from τ = 0, as seen in Figure 8b, the flow changes from two inward bulk motions to two repelling flows. The temporal gap allows for the partial overlap of B_1's growth and B_2's collapse leading to the formation of the conical shape in B_2 that reverses into its own walls and generates a sharp outward flow. Further increase in the phase until τ = 1, (Figure 8c), concentrates more mass flow in one direction, and B_1's flow becomes more defined while the opposing side remains a slower bulk flow. When B_2 is initiated at B_1's maximum size (Figure 8c @ 56.8 μs), the bubble becomes elongated as with a smaller phase difference (Figure 8b), but the arrangement allows for a stronger effect. Further increasing the BB phase past τ = 1 (Figure 8d) decreases

AIP Publishing

ACCEPTED MANUSCRIPT
Physics of Fluids
This is the author's peer reviewed, accepted manuscript. However, the online version of record will be different from this version once it has been copyedited and typeset.
PLEASE CITE THIS ARTICLE AS DOI:10.1063/5.0007164

the strength of the formed jet due to a shorter exposure to the high pressures generated during the alignment of B_1's collapse and B_2's maximum size. A notable difference between an approximately equal positive and negative phase shift from the optimum antiphase arrangement, is on the shape of the jet. For jet-forming phases smaller than τ = 1, the jet has a focused, pointed shape which can propagate at faster speeds most notable in Figure 9 which shows the jet evolution over time and maximum speeds achieved at variable BB phases.

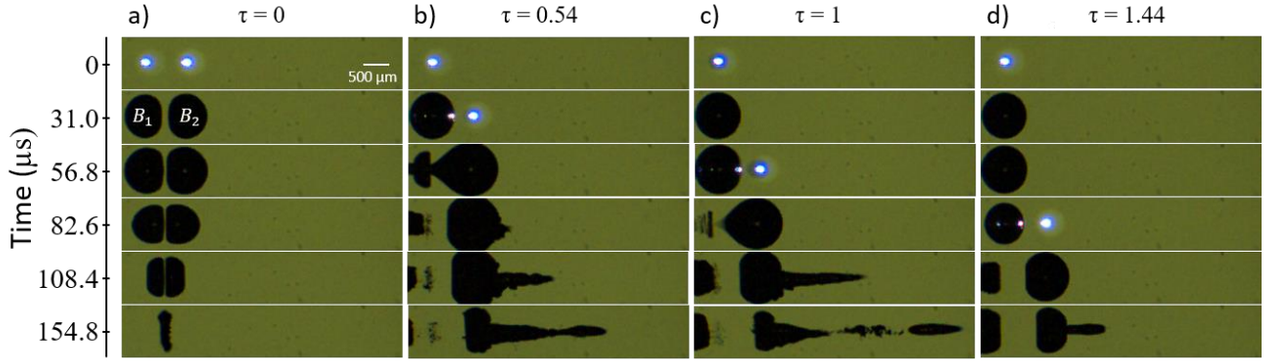

Figure 8. Image sequence of four different phase separations: τ = a) 0, b) 0.54, c) 1, and d) 1.44 (each at $\gamma_{BB} = 0.74, \rho = 1$). Time 0 shows the moment that Laser 1 is fired.

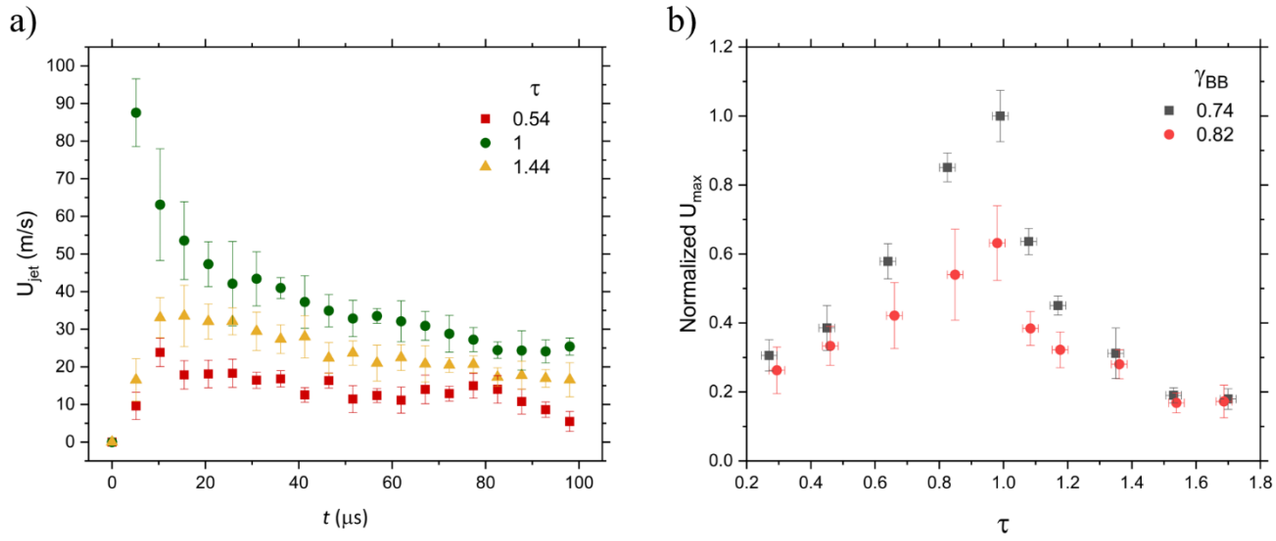

Figure 9. a) Jet speed with respect to time of jet formation for three different BB initiation phases (at $\gamma_{BB} = 0.74, \rho = 1$). b) normalized maximum jet speed for various bubble-bubble phase separations.

The three phases shown in Figure 9 are chosen for representing the peak jet speed reached at τ = 1, and comparable delays of $\Delta\tau \approx \pm 0.45$. As observed in Figure 9 a, a delay before and after the optimal phase do not lead to the same diminishing effects. A shorter delay leads to a higher converged velocity (U_{conv}~18 m/s) than the same displaced delay above the optimal phase (U_{conv} ~11 m/s). This may be explained by the different pressure conditions during the formation and propagation of the jet. For jets formed at phases smaller than τ = 1, the growth of B_2 coincides with the full collapse of B_1 and is thus pulled and elongated. For jets $\tau \geq 1$, the growth of B_2 partially overlaps with both the collapse and regrowth of B_1. Thus, B_2 is not maximally elongated and the emerging jet is not accelerated at the same rate. This suggests that to minimize change of speed from errors, it is best to underestimate the expansion time and be to the left of the optimal point. Differences can be further noted by comparing the time constants of the exponential growth, $C_{growth} = 0.53$, and exponential decay, $C_{growth} = 0.26$. The phase of τ = 1 has the largest velocity error bar because the jet tip of the highest speeds can be within the bubble shadow and emerge at variable times for each experiment.

[1] F. Reuter and R. Mettin, Ultrason. Sonochem. **29**, 550 (2016).

[2] C.D. Ohl, M. Arora, R. Dijkink, V. Janve, and D. Lohse, Appl. Phys. Lett. **89**, (2006).

AIP Publishing

ACCEPTED MANUSCRIPT

Physics of Fluids

This is the author's peer reviewed, accepted manuscript. However, the online version of record will be different from this version once it has been copyedited and typeset.
PLEASE CITE THIS ARTICLE AS DOI:10.1063/5.0007164

[3] B. Verhaagen and D. Fernández Rivas, Ultrason. Sonochem. **29**, 619 (2016).

[4] R. Dijkink, S. Le Gac, E. Nijhuis, A. Van Den Berg, I. Vermes, A. Poot, and C.D. Ohl, Phys. Med. Biol. **53**, 375 (2008).

[5] Y. Arita, M. Ploschner, M. Antkowiak, F. Gunn-Moore, and K. Dholakia, Opt. Lett. **38**, 3402 (2013).

[6] C. Wei, J. Xia, M. Lombardo, C. Perez, B. Arnal, K. Larson-Smith, I. Pelivanov, T. Matula, L. Pozzo, and M. O'Donnell, Opt. Lett. **39**, 2599 (2014).

[7] S.D. George, S. Chidangil, and D. Mathur, Langmuir **35**, 10139 (2019).

[8] N. Zamora-Romero, V. Robles, C. Alvarez, N. Cuando-Espitia, L.F. Devia-Cruz, E. Penilla, D.L. Halaney, and G. Aguilar, Opt. InfoBase Conf. Pap. **Part F61-E**, 1041707 (2017).

[9] D. Banks, V. Robles, B. Zhang, L.F. Devia-Cruz, S. Camacho-Lopez, and G. Aguilar, Exp. Therm. Fluid Sci. **103**, 385 (2019).

[10] B. Liu, J. Cai, and X. Huai, Int. J. Heat Mass Transf. **78**, 830 (2014).

[11] W. Lauterborn and H. Bolle, J. Fluid Mech. **72**, 391 (1975).

[12] E.A. Brujan, G.S. Keen, A. Vogel, and J.R. Blake, Phys. Fluids **14**, 85 (2002).

[13] G.Y. Yuan, B.Y. Ni, Q.G. Wu, Y.Z. Xue, and A.M. Zhang, J. Fluids Struct. **92**, (2020).

[14] L. Van Wijngaarden, Ultrason. Sonochem. **29**, 524 (2016).

[15] P.A. Barnes and K.E. Rieckhoff, Appl. Phys. Lett. **13**, 282 (1968).

[16] A. Vogeland and W. Lauterborn, J. Acoust. Soc. Am. **84**, 719 (1988).

[17] R. Timm, J. Fluid Mech. **206**, 299 (1989).

[18] C. Lechner, W. Lauterborn, M. Koch, and R. Mettin, Phys. Rev. Fluids **4**, (2019).

[19] E.A. Brujan, K. Nahen, P. Schmidt, and A. Vogel, J. Fluid Mech. **433**, 251 (2001).

[20] E.A. Brujan, K. Nahen, P. Schmidt, and A. Vogel, J. Fluid Mech. **433**, 283 (2001).

[21] D. Horvat, U. Orthaber, J. Schille, L. Hartwig, U. Löschner, A. Vrečko, and R. Petkovšek, Int. J. Multiph. Flow **100**, 119 (2018).

[22] A. Vogel and V. Venugopalan, Chem. Rev. **103**, 577 (2003).

[23] W. Xu, Y. Zhai, J. Luo, Q. Zhang, and J. Li, Exp. Therm. Fluid Sci. **109**, 109897 (2019).

[24] B. Han, K. Köhler, K. Jungnickel, R. Mettin, W. Lauterborn, and A. Vogel, J. Fluid Mech. **771**, 706 (2015).

[25] L.W. Chew, E. Klaseboer, S.W. Ohl, and B.C. Khoo, Phys. Rev. E - Stat. Nonlinear, Soft Matter Phys. **84**, (2011).

[26] C.T. Hsiao, J.K. Choi, S. Singh, G.L. Chahine, T.A. Hay, Y.A. Ilinskii, E.A. Zabolotskaya, M.F. Hamilton, G. Sankin, F. Yuan, and P. Zhong, J. Fluid Mech. **716**, 137 (2013).

[27] J.C. Stachowiak, T.H. Li, A. Arora, S. Mitragotri, and D.A. Fletcher, J. Control. Release **135**, 104 (2009).

[28] J. Baxter and S. Mitragotri, J. Control. Release **106**, 361 (2005).

[29] V. Menezes, S. Kumar, and K. Takayama, J. Appl. Phys. **106**, 1 (2009).

AIP Publishing

ACCEPTED MANUSCRIPT

[30] C. Berrospe-Rodriguez, C.W. Visser, S. Schlautmann, D.F. Rivas, and R. Ramos-Garcia, J. Biomed. Opt. **22**, 1 (2017).

[31] Y. Tagawa, N. Oudalov, C.W. Visser, I.R. Peters, D. van der Meer, C. Sun, A. Prosperetti, and D. Lohse, Phys. Rev. X **2**, 1 (2012).

[32] T.H. Han and J.J. Yoh, J. Appl. Phys. **107**, 1 (2010).

[33] N. Kyriazis, P. Koukouvinis, and M. Gavaises, Proc. R. Soc. A Math. Phys. Eng. Sci. **475**, (2019).

[34] M. Moradiafrapoli and J.O. Marston, Chem. Eng. Res. Des. **117**, 110 (2017).

[35] L. Oyarte Gálvez, M. Brió Pérez, and D. Fernández Rivas, J. Appl. Phys. **125**, 14 (2019).

[36] R. Zaca-Morán, J. Castillo-Mixcóatl, N.E. Sierra-González, J.M. Pérez-Corte, P. Zaca-Morán, J.C. Ramírez-San-Juan, R. Ramos-García, and J.P. Padilla-Martínez, Opt. Express **28**, 4928 (2020).

[37] J.P. Padilla-Martinez, C. Berrospe-Rodriguez, G. Aguilar, J.C. Ramirez-San-Juan, and R. Ramos-Garcia, Phys. Fluids **26**, (2014).

[38] S.F. Rastopov and A.T. Sukhodolsky, in *USSR Acad. Sci.* (1990), pp. 127–134.

[39] H. Jang, E. Hur, Y. Kim, S.-H. Lee, N.G. Kang, and J.J. Yoh, J. Biomed. Opt. **19**, 118002 (2014).

[40] P.A. Quinto-Su, M. Suzuki, and C.D. Ohl, Sci. Rep. **4**, 1 (2014).

[41] Z. Han, J. Li, M. Singh, C. Wu, C.H. Liu, S. Wang, R. Idugboe, R. Raghunathan, N. Sudheendran, S.R. Aglyamov, M.D. Twa, and K. V. Larin, Phys. Med. Biol. **60**, 3531 (2015).

[42] X. Liang, IEEE Trans Biomed Eng. **57**, 953 (2013).

[43] I. Akhatov, O. Lindau, A. Topolnikov, R. Mettin, N. Vakhitova, and W. Lauterborn, Phys. Fluids **13**, 2805 (2001).

[44] P.K. Kennedy, D.X. Hammer, and B.A. Rockwell, Prog. Quantum Electron. **21**, 155 (1997).

[45] G.H. Goldsztein, Stud. Appl. Math. **112**, 101 (2004).

[46] J. Schramm and S. Mitragotri, Pharm. Res. **19**, 1673 (2002).

[47] K. Cu, R. Bansal, S. Mitragotri, and D. Fernandez Rivas, Ann. Biomed. Eng. (2019).

[48] E.L. Giudice and J.D. Campbell, Adv. Drug Deliv. Rev. **58**, 68 (2006).

[49] M. Ahearne, Y. Yang, A.J. El Haj, K.Y. Then, and K.K. Liu, J. R. Soc. Interface **2**, 455 (2005).

Physics of Fluids

This is the author's peer reviewed, accepted manuscript. However, the online version of record will be different from this version once it has been copyedited and typeset.
PLEASE CITE THIS ARTICLE AS DOI: 10.1063/5.0007164

AIP Publishing

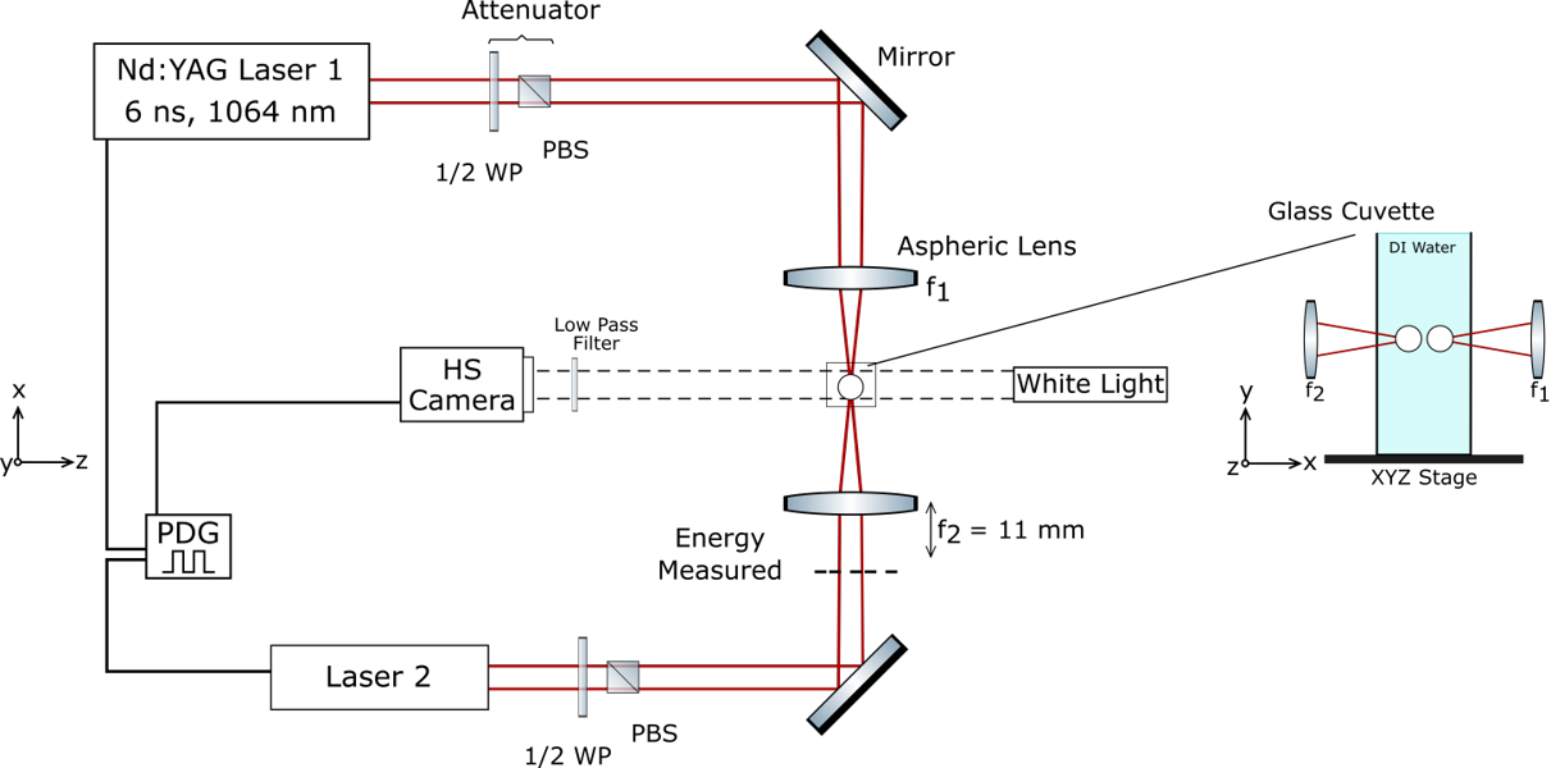
Attenuator
Nd:YAG Laser 1
6 ns, 1064 nm
Mirror
PBS
1/2 WP
Glass Cuvette
Aspheric Lens
f_1
DI Water
Low Pass
Filter
HS
Camera
White Light
f_2
f_1
x
y
z
y
z
x
XYZ Stage
PDG
f_2 = 11 mm
Energy
Measured
Laser 2
PBS
1/2 WP

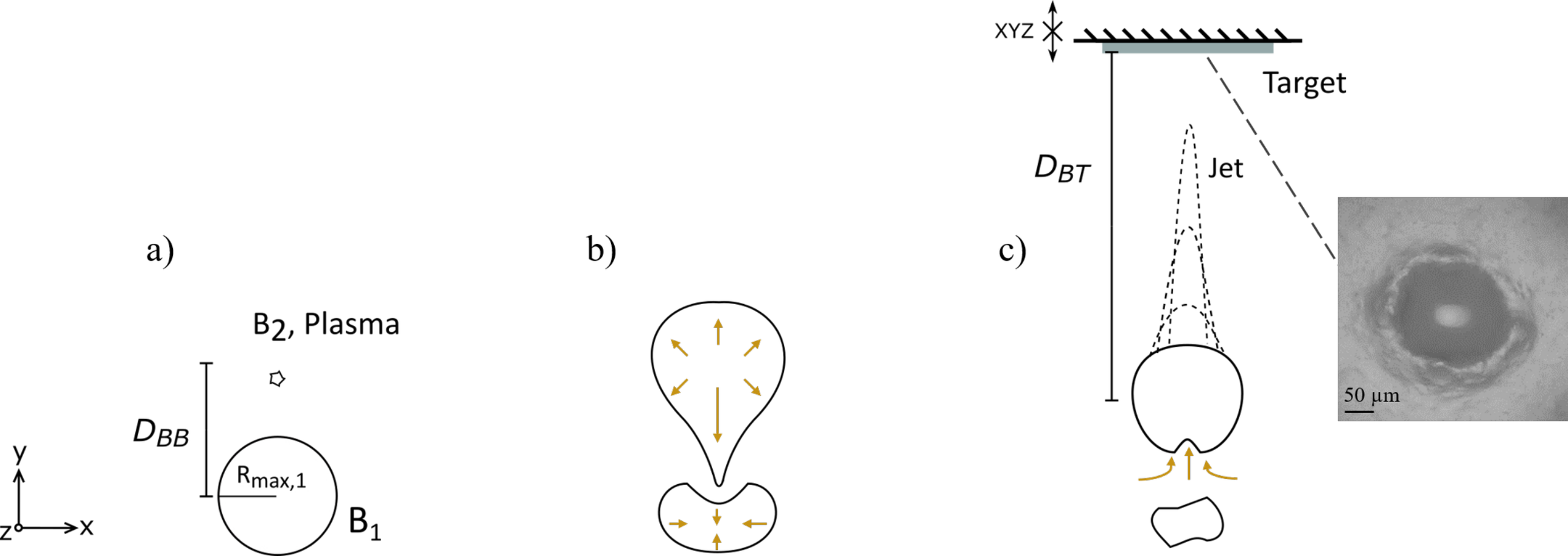
a)
B2, Plasma
DBB
Rmax,1
B1
y
z
x
b)
c)
XYZ
Target
DBT
Jet
50 µm

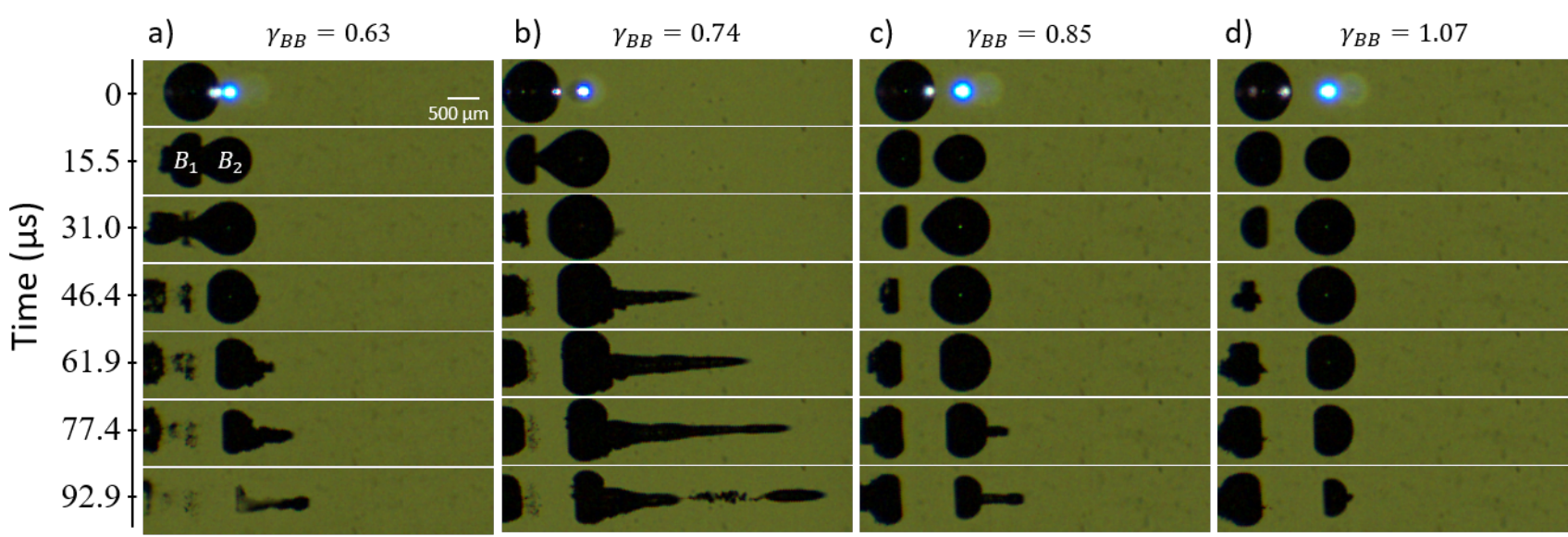
a)
$\gamma_{BB} = 0.63$
b)
$\gamma_{BB} = 0.74$
c)
$\gamma_{BB} = 0.85$
d)
$\gamma_{BB} = 1.07$
Time (μs)
0
15.5
31.0
46.4
61.9
77.4
92.9
500 μm
B_1
B_2

a)

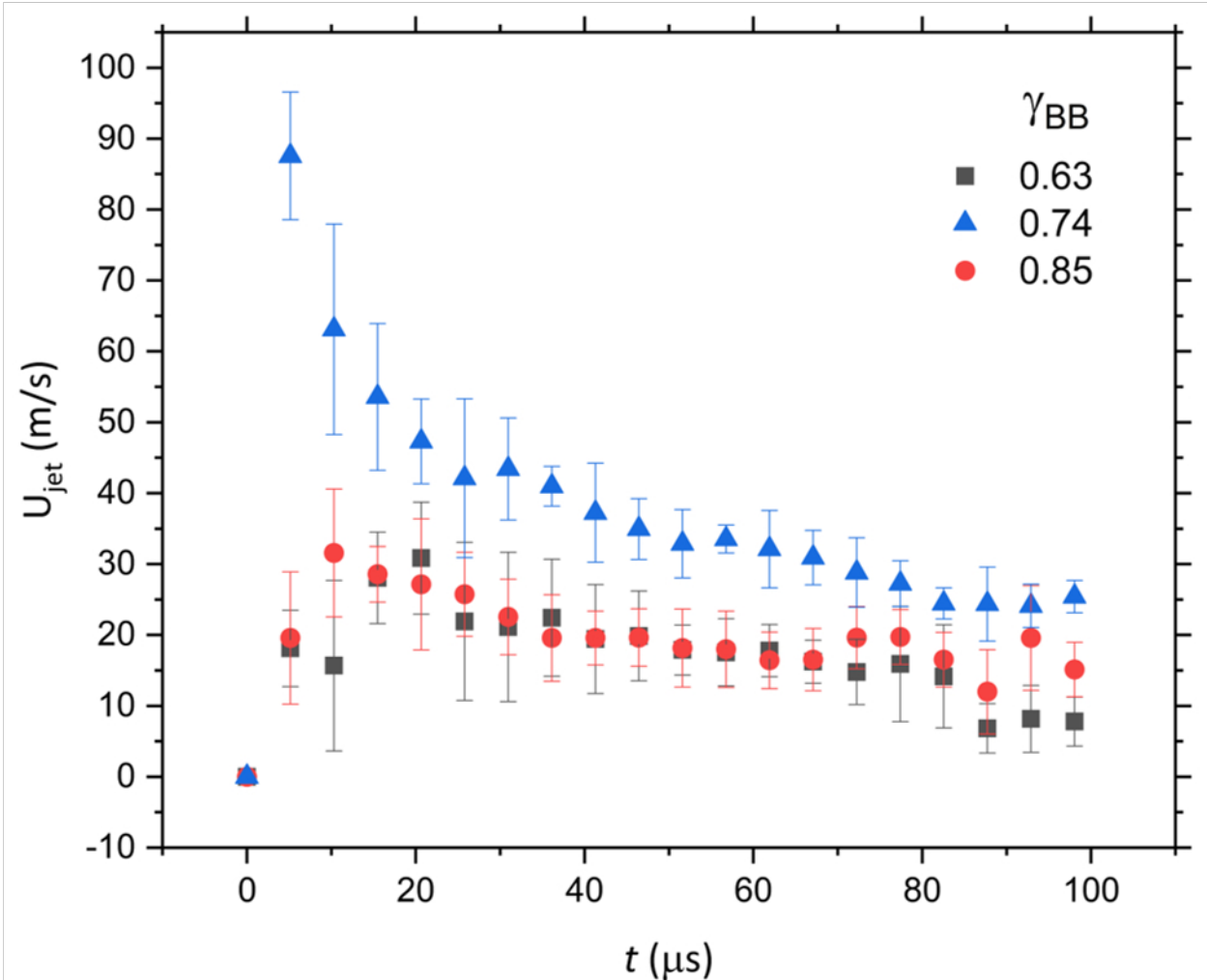
γ_{BB}
0.63
0.74
0.85
U_{jet} (m/s)
t (μs)
100
90
80
70
60
50
40
30
20
10
0
-10
0
20
40
60
80
100

b)

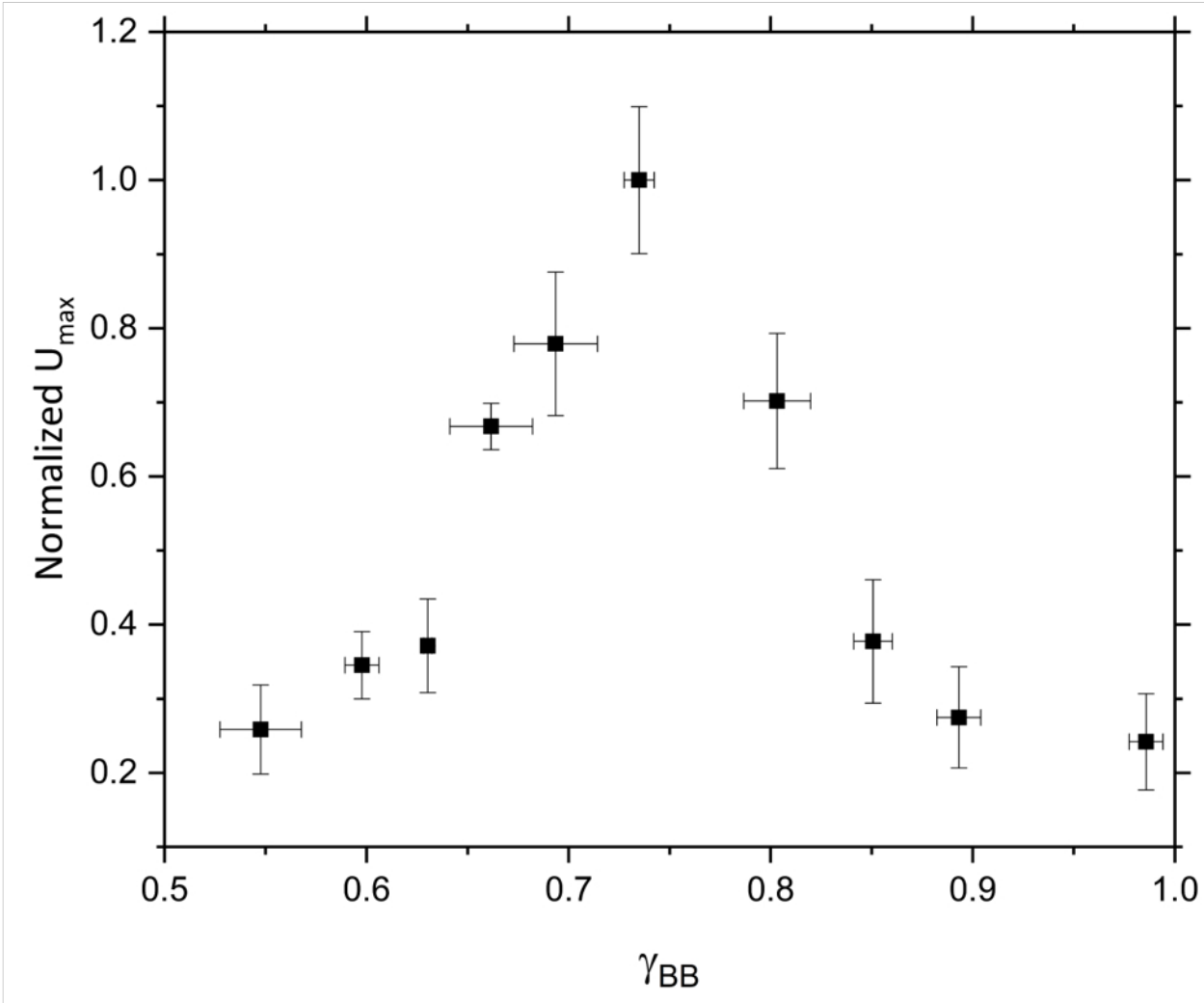

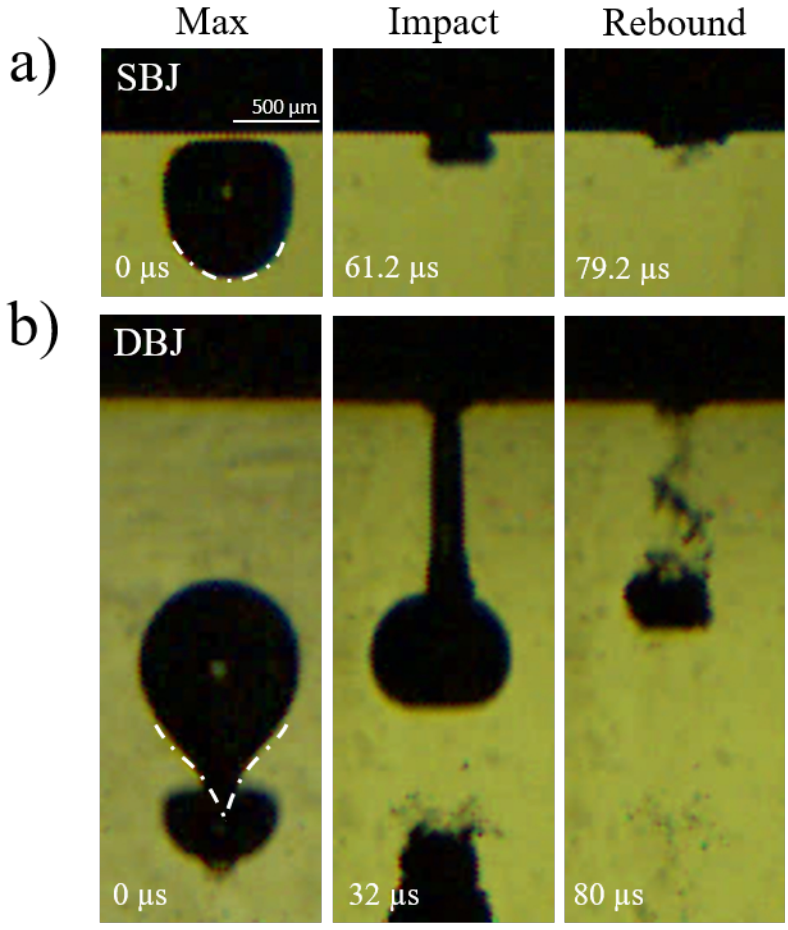
Max
Impact
Rebound
a)
SBJ
500 μm
0 μs
61.2 μs
79.2 μs
80 μm
D_R
b)
DBJ
0 μs
32 μs
80 μs
80 μm

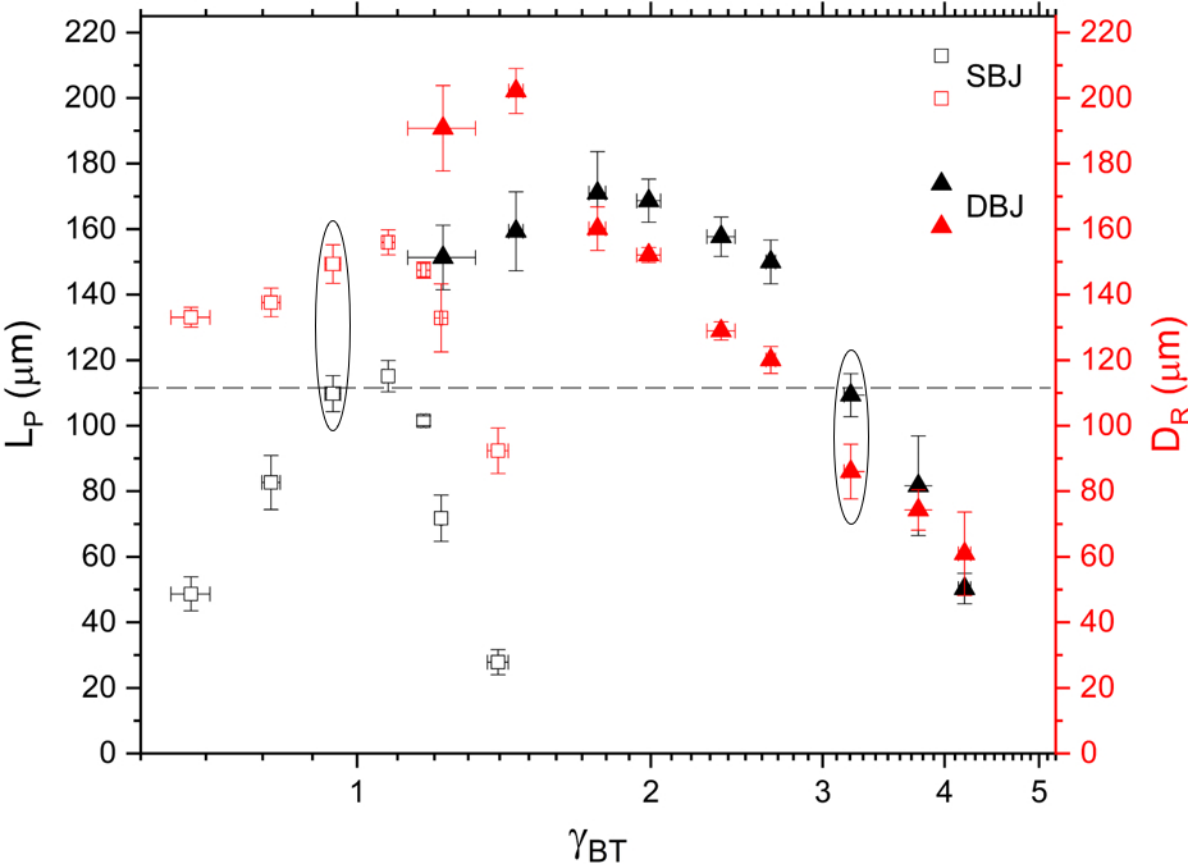
SBJ
DBJ
L_P (μm)
D_R (μm)
γ_{BT}
0
20
40
60
80
100
120
140
160
180
200
220
1
2
3
4
5

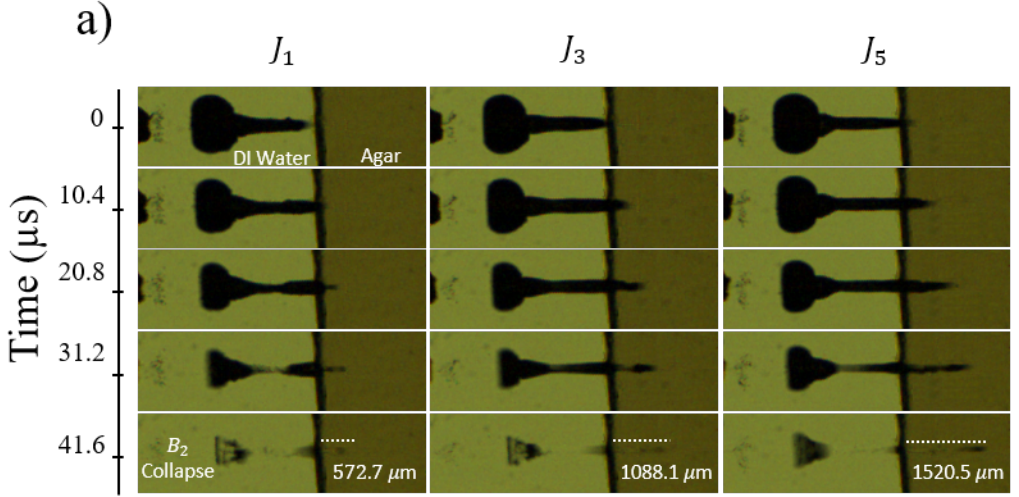
a)
J_1
J_3
J_5
Time (μs)
0
10.4
20.8
31.2
41.6
DI Water
Agar
B_2
Collapse
572.7 μm
1088.1 μm
1520.5 μm

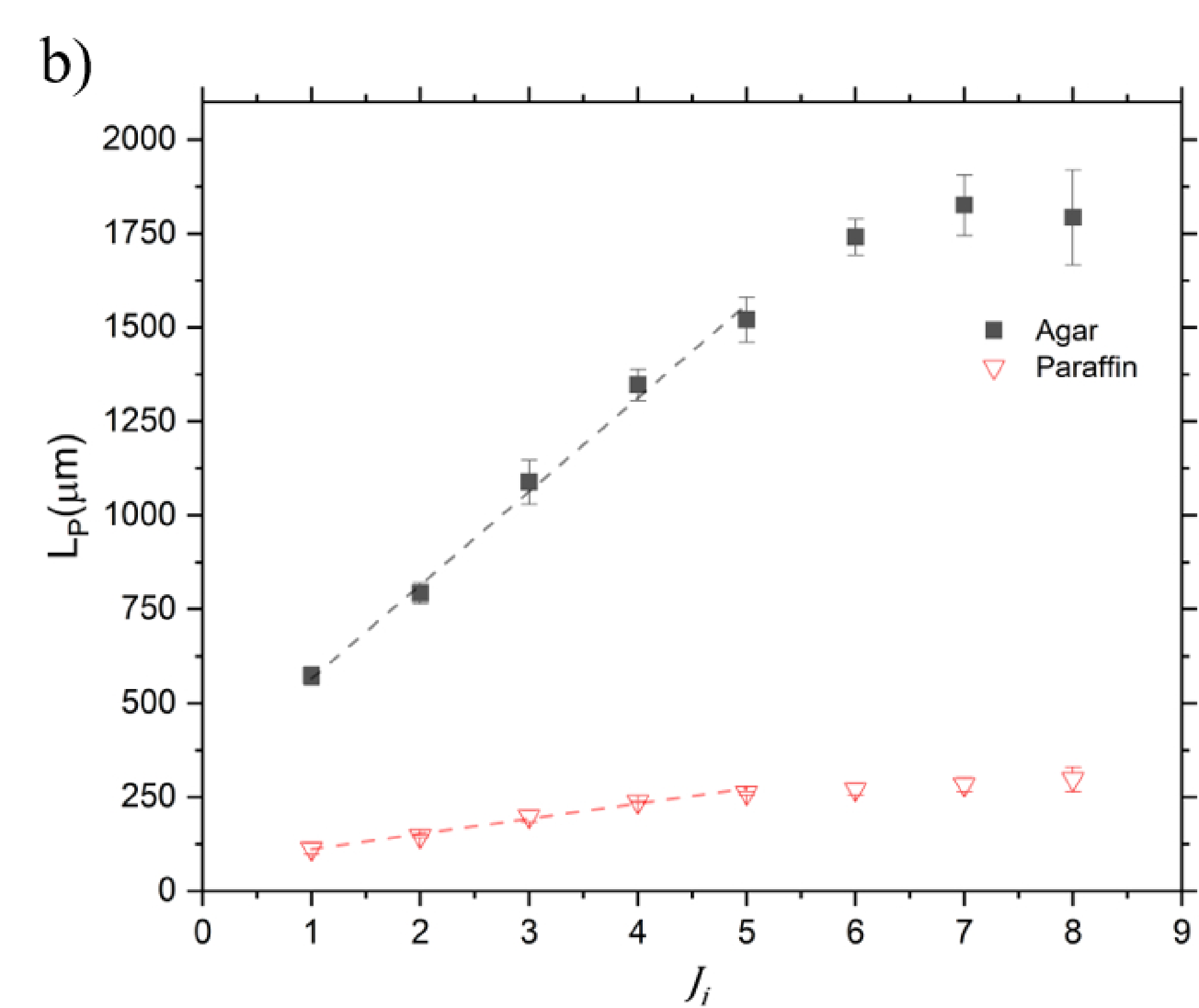
b)
2000
1750
1500
1250
1000
750
500
250
0
$L_P(\mu m)$
0
1
2
3
4
5
6
7
8
9
J_i
Agar
Paraffin

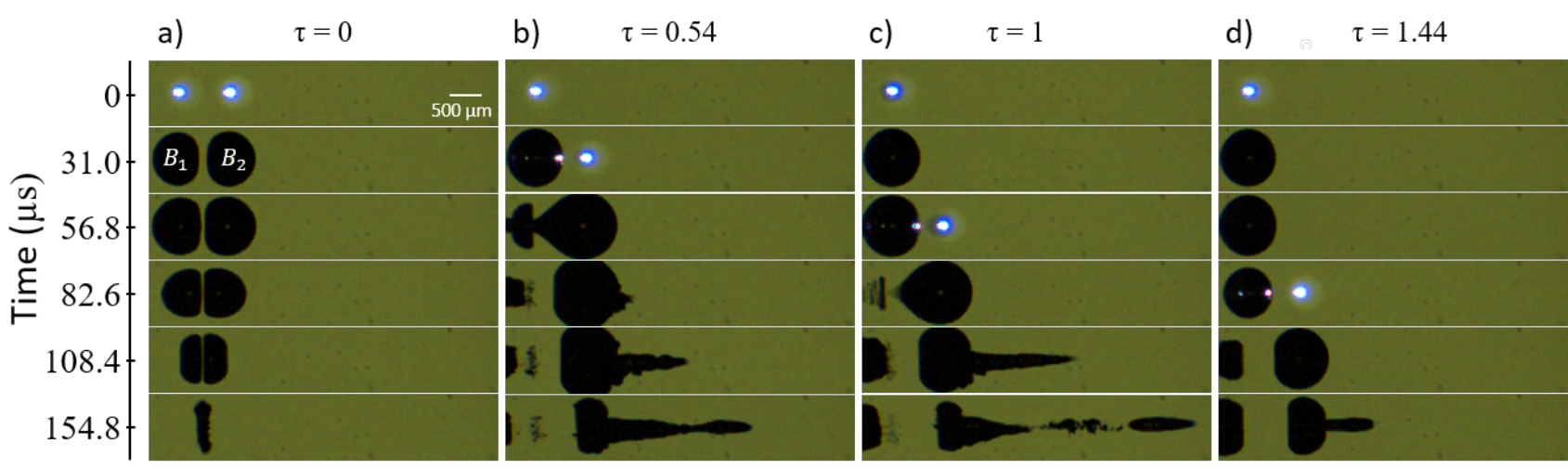
a)
τ = 0
b)
τ = 0.54
c)
τ = 1
d)
τ = 1.44
500 μm
B_1
B_2
Time (μs)
0
31.0
56.8
82.6
108.4
154.8

a)

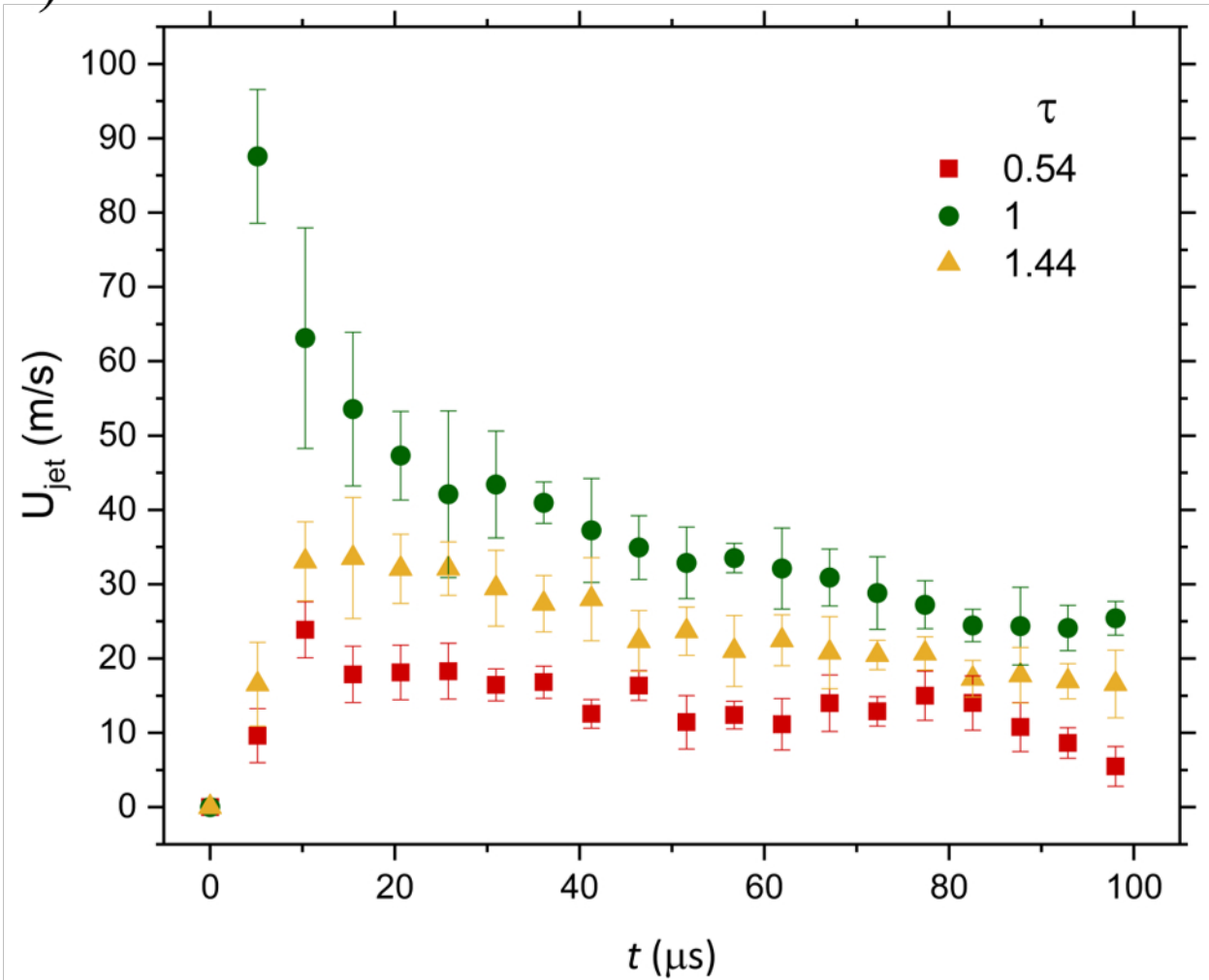
τ
0.54
1
1.44
U_{jet} (m/s)
t (μs)
0
10
20
30
40
50
60
70
80
90
100
0
20
40
60
80
100

b)

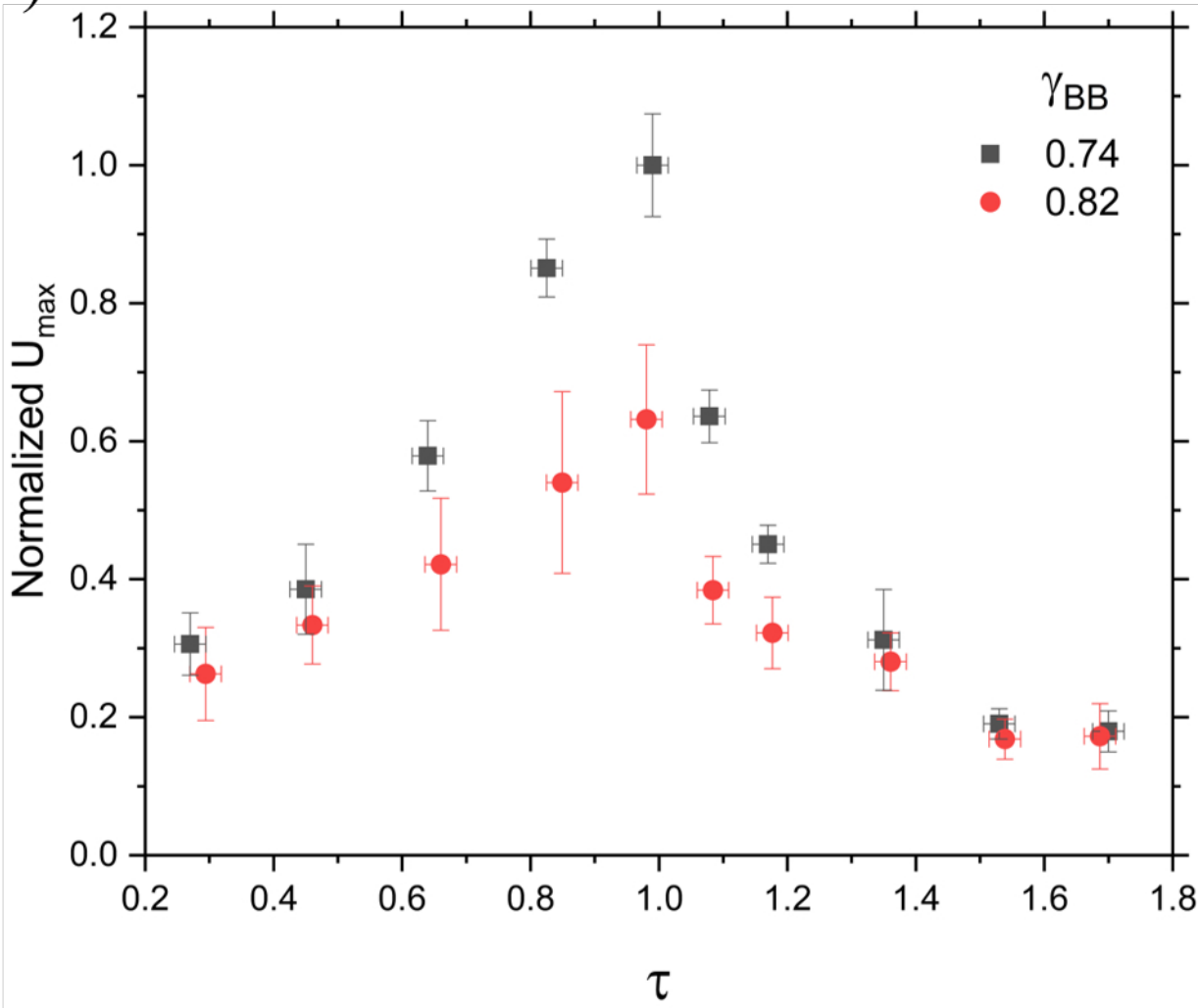
Normalized U_{max}
τ
γ_{BB}
0.74
0.82
0.0
0.2
0.4
0.6
0.8
1.0
1.2
0.2
0.4
0.6
0.8
1.0
1.2
1.4
1.6
1.8